V772 Cas: an ellipsoidal HgMn star in an eclipsing binary

O. Kochukhov[1]★, C. Johnston[2], J. Labadie-Bartz[3], S. Shetye[4], T. A. Ryabchikova[5], A. Tkachenko[2], M. E. Shultz[6]

[1]*Department of Physics and Astronomy, Uppsala University, Box 516, Uppsala 75120, Sweden*
[2]*Instituut voor Sterrenkunde, KU Leuven, Celestijnenlaan 200D, 3001, Leuven, Belgium*
[3]*Instituto de Astronomia, Geofísica e Ciencias Atmosféricas, Universidade de Sào Paulo, Rua do Matão 1226, Cidade Universitãria, Sáo Paulo, SP 05508-900, Brazil*
[4]*Institute of Astronomy and Astrophysics (IAA), Université Libre de Bruxelles (ULB), CP 226, Boulevard du Triomphe,1050 Bruxelles, Belgium*
[5]*Institute of Astronomy, Russian Academy of Sciences, Pyatnitskaya 48, 119017 Moscow, Russia*
[6]*Department of Physics and Astronomy, University of Delaware, 217 Sharp Lab, Newark, Delaware, 19716, USA*

Accepted XXX. Received YYY; in original form ZZZ

ABSTRACT

The late B-type star V772 Cas (HD 10260) was previously suspected to be a rare example of a magnetic chemically peculiar star in an eclipsing binary system. Photometric observations of this star obtained by the TESS satellite show clear eclipses with a period of 5.0137 d accompanied by a significant out-of-eclipse variation with the same period. High-resolution spectroscopy reveals V772 Cas to be an SB1 system, with the primary component rotating about a factor two slower than the orbital period and showing chemical peculiarities typical of non-magnetic HgMn chemically peculiar stars. This is only the third eclipsing HgMn star known and, owing to its brightness, is one of the very few eclipsing binaries with chemically peculiar components accessible to detailed follow-up studies. Taking advantage of the photometric and spectroscopic observations available for V772 Cas, we performed modelling of this system with the PHOEBE code. This analysis provided fundamental parameters of the components and demonstrated that the out-of-eclipse brightness variation is explained by the ellipsoidal shape of the evolved, asynchronously rotating primary. This is the first HgMn star for which such variability has been definitively identified.

Key words: stars: individual: V772 Cas (HD 10260) – stars: early-type – stars: binaries: eclipsing – stars: chemically peculiar

1 INTRODUCTION

About 10 per cent of A and B main sequence stars possess stable, globally organised magnetic fields with a strength of at least 300 G (Aurière et al. 2007; Sikora et al. 2019). These stars typically exhibit anomalous absorption spectra, shaped by surface overabundances of Si, Fe-peak, and rare-earth elements, and are known as magnetic chemically peculiar or ApBp stars. The process of radiatively driven atomic diffusion (Michaud et al. 2015) responsible for these abundance anomalies also produces a high-contrast, long-lived non-uniform horizontal distribution of chemical elements. Local variation of metal abundances associated with these chemical spots modifies emergent stellar radiation and leads to a characteristic photometric rotational modulation known as α^2 CVn (ACV) type of stellar variability (Samus' et al. 2017).

The properties of magnetic fields of ApBp stars do not depend on stellar mass or rotation rate, making them strikingly different from characteristics of the dynamo-generated fields observed in late-type stars (e.g. Vidotto et al. 2014). It is believed that the strong fields found in early-type stars are dynamically stable, 'fossil' remnants of the magnetic flux generated or acquired by these stars at some earlier evolutionary phase (Braithwaite & Spruit 2004; Neiner et al. 2015). The origin of fossil fields is not understood. This magnetic flux might be inherited from molecular clouds at stellar birth (Mestel 1999), produced by the convective dynamo during pre-main sequence evolution (Moss 2004) or created by a short-lived dynamo operating during stellar merger events (Schneider et al. 2019).

The binary characteristics of early-type magnetic stars may provide crucial clues, allowing one to test alternative fossil field hypotheses. The non-magnetic chemically peculiar stars of Am (A-type stars with enhanced lines of Fe-peak elements) and HgMn (late-B stars identified by strong lines of Hg and/or Mn) types are frequently found in close binaries (Gerbaldi, Floquet & Hauck 1985; Ryabchikova 1998; Carquillat & Prieur 2007), including eclipsing systems (Nordstrom & Johansen 1994; Strassmeier et al. 2017; Takeda et al. 2019). In contrast, only about ten close ($P_{\rm orb}$ < 20 d) spectroscopic binaries containing at least one magnetic ApBp star are known (Landstreet et al. 2017). The overall incidence rate of magnetic upper main sequence stars in close binaries is less than 2 per cent (Alecian et al. 2015), although this fraction is significantly higher if one includes wide long-period systems (Mathys 2017). This low incidence of magnetic ApBp stars in close binaries is frequently considered as an argument in favour of the stellar merger origin of fossil fields (de Mink et al. 2014; Schneider et al. 2016). In this context, confirmation of magnetic ApBp stars in short-period binary systems gives support to alternative theories or, at least, demonstrates that early-type stars

★ E-mail: oleg.kochukhov@physics.uu.se

may acquire magnetic fields through different channels. In addition, detached close binary stars, particularly those showing eclipses, are valuable astrophysical laboratories that provide model independent stellar parameters and allow one to study pairs of co-evolving stars formed in the same environment. Until recently, no early-type magnetic stars in eclipsing binaries were known. The first such system, HD 66051, was identified by Kochukhov et al. (2018). The second system, HD 62658 containing twin components of which only one is magnetic, was found by Shultz et al. (2019). Several other eclipsing binaries containing candidate ApBp stars were proposed (Hensberge et al. 2007; González, Hubrig & Castelli 2010; Skarka et al. 2019), but the magnetic nature of these stars has not been verified by direct detections of their fields using the Zeeman effect. In this paper we put a spotlight on another candidate eclipsing magnetic Bp star, which received little attention prior to our work despite being significantly brighter than the confirmed magnetic eclipsing systems HD 62658 and HD 66051.

V772 Cas (HR 481, HD 10260, HIP 7939) is a bright (V = 6.7) but little studied chemically peculiar late-B star. The exact type of its spectral peculiarity is uncertain. Cowley (1972) classified this star as B8IIIpSi whereas Dworetsky (1976) considered it an HgMn star. Both studies used low-dispersion classification spectra. The former BpSi classification appears to be more common in recent literature (e.g. Gandet 2008; Renson & Manfroid 2009; Skarka et al. 2019). The variable star designation comes from Kazarovets et al. (1999), who suggested this object to be an α^2 CVn-type variable based on the Hipparcos epoch photometry (Perryman et al. 1997). Otero (2007) discovered eclipses in the Hipparcos light curve. This analysis was improved by Gandet (2008). He confirmed the presence of primary eclipses, derived an orbital period of 5.0138 d and demonstrated that archival photographic radial velocity measurements (Hube 1970) show coherent variation with the same period. These results, along with the B8IIIpSi spectral classification and an evidence of the out-of-eclipse variability, led Gandet (2008) to suggest V772 Cas as an α^2 CVn variable in a short-period eclipsing binary – an exceptionally rare and interesting object akin to the recently discovered magnetic eclipsing binaries HD 66051 and HD 62658. Apart from the study by Huang, Gies & McSwain (2010), who determined $T_{\rm eff}$ = 13188 ± 250 K and $\log g$ = 3.43 ± 0.05 from the low-resolution hydrogen Balmer line spectra, no model atmosphere and/or abundance analysis was carried out for V772 Cas. In fact, to the best of our knowledge, this star was never studied with high-resolution spectra.

In this paper we present a detailed photometric and spectroscopic investigation of V772 Cas that provides a new insight into the nature of this star. In Sect. 2 we describe the new observational data used in our study. Orbital modelling and derivation of the binary component parameters are presented in Sect. 3. Model atmosphere parameters and chemical abundances of the primary are determined in Sect. 4. The paper concludes with the discussion in Sect. 5.

2 OBSERVATIONS

2.1 Space photometry

The NASA Transiting Exoplanet Survey Satellite (TESS; Ricker et al. 2015) began its nominal 2 year mission in 2018 to discover Earth-sized transiting exoplanets. Using four cameras that cover a combined field of view of 24° × 96° and a red filter that records light in the range 6000 to 10500Å, both ecliptic hemispheres are surveyed for one year each, in 13 sectors that extend from the ecliptic plane to the pole. Each sector is observed for approximately 27.5 days, and a given field on the sky can be observed in multiple sectors if it falls on overlap regions. Nominal TESS targets are bright, with I_c magnitudes between 4 and 13, with a noise floor of approximately 60 ppm hr^{-1}.

Full Frame Images (FFIs) from TESS are available at a 30-minute cadence for the entire field of view, allowing light curves to be extracted for all objects that fall on the detector. Certain high priority targets were pre-selected by the TESS mission to be observed with 2-minute cadence, some of which were chosen from guest investigator programs.

V772 Cas was observed in cycle 2 of the TESS mission in sector 18 (2019-Nov-02 to 2019-Nov-27) in 30-minute cadence mode (and was not pre-selected for 2-minute cadence observations; TESS Input Catalog ID: 444833007). A target pixel file of a 50 × 50 grid of pixels centered on V772 Cas was downloaded with TESScut[1] (Brasseur et al. 2019), with further processing aided by the LIGHTKURVE package (Lightkurve Collaboration et al. 2018). A light curve for V772 Cas was extracted with aperture photometry using an aperture of 36 pixels centred on the target. This aperture was chosen to minimise contaminating flux from neighbouring stars, which would otherwise bias the binary system modelling and possibly introduce additional signals from other sources, while still achieving a high signal-to-noise ratio. A principal component analysis routine was then applied to the extracted light curve to detrend against signals common to neighbouring pixels (outside of a 15 × 15 pixel exclusion zone). After removing outliers and data points more prone to systematic effects (mostly scattered light near TESS orbital perigee), the light curve includes 958 observations spanning 22.1 days.

The Hipparcos light curve analysed by Otero (2007) and Gandet (2008) covered 233 orbital cycles with about a dozen photometric data points tracing the primary eclipse. Although the TESS data corresponds to a time span of just 4.4 orbits, it samples the eclipses much more densely owing to its higher measurement cadence. Moreover, individual TESS measurements are about a factor of 200 more precise than the Hipparcos photometry.

2.2 High-resolution spectroscopy

We obtained high-resolution spectra of V772 Cas using the High-Efficiency and high-Resolution Mercator Échelle Spectrograph (HERMES) mounted on the 1.2 m Mercator telescope at the Observatorio del Roque de los Muchachos, La Palma, Canary Islands, Spain. This instrument provides coverage of the 3700–9100 Å wavelength region at a resolving power of 85 000 (Raskin et al. 2011). The star was observed on five consecutive nights, from January 27 to January 31, 2020, with two spectra obtained on each night. Exposure times of 600–800 s were used, yielding a signal-to-noise ratio (S/N) of 190–280 per ≈ 0.03 Å pixel of the extracted spectrum in the wavelength interval from 5000 to 5500 Å. The HERMES pipeline reduction software was employed to perform the basic échelle data reduction steps, including the bias and flat field corrections, extraction of one-dimensional spectra and wavelength calibration. The resulting merged, un-normalised spectra were then normalised to the continuum with the methodology described by Rosén et al. (2018).

The log of ten HERMES observations of V772 Cas is given in Table 1. The first four columns of this table list the UT date of observation, the corresponding heliocentric Julian date, the orbital phase calculated according to the ephemeris derived in Sect. 3, and

[1] https://mast.stsci.edu/tesscut/

the S/N ratio. The last column provides radial velocities determined in the next section.

2.3 Spectroscopic classification and radial velocity measurements

Initial qualitative analysis of the high-resolution spectra of V772 Cas showed the presence of a single set of spectral lines with variable radial velocity and line strengths typical of HgMn late-B chemically peculiar stars. Specifically, the HgMn classification of this star is unambiguously demonstrated by the presence of Hg II 3984 Å, Ga II 6334 Å and numerous strong Mn II and P II lines. On the other hand, ionised Si lines are not anomalously strong and rare-earth absorption features are not prominent in the spectrum of V772 Cas, which argues against identification of this object as a Si-peculiar Bp star.

Based on this initial assessment, we extracted a line list from the VALD database (Ryabchikova et al. 2015; Pakhomov, Ryabchikova & Piskunov 2019) with the chemical abundances typical of HgMn stars (Ghazaryan, Alecian & Hakobyan 2018) and model atmosphere parameters $T_{\rm eff}$ = 13000 K, log g = 3.5, close to the values reported by Huang et al. (2010)[2]. This line list was employed for calculation of least-squares deconvolved (LSD) profiles (Kochukhov, Makaganiuk & Piskunov 2010) with the goal to study the radial velocity variation of the primary and search for spectral signatures of the secondary. The LSD profiles were constructed by combining 1094 metal lines deeper than 5 per cent of the continuum. These average spectra are illustrated in Fig. 1, where the data are phased with the orbital ephemeris $HJD = 2458803.4016 + 5.0138 \times E$ determined below (Sect. 3).

The radial velocity of the primary was measured from the LSD profiles with the help of the centre-of-gravity method. These measurements made use of the ±30 km s^{-1} velocity range around the line centre. The resulting radial velocity changes from −37 to 38 km s^{-1}. This variation is coherent on the 5 d time-scale covered by the spectroscopic observations and is consistent with the orbital period seen in photometry. Individual radial velocities are reported in the last column of Table 1. The formal uncertainty of these measurements is 50–60 m s^{-1}.

At the same time, no evidence of a spectral contribution of the secondary was found in the LSD profiles. This is not surprising considering the luminosity ratio of > 100 estimated from the eclipse depths in the TESS light curve. We tested alternative solar-composition LSD line masks for $T_{\rm eff}$ of 7000, 9000, and 11000 K but still could not detect any features in the LSD profile time series that could be attributed to the secondary component.

Table 1. Log of spectroscopic observations of V772 Cas.

UT date	HJD	Orbital phase	S/N (pixel^{-1})	$V_{\rm r}$ (km s^{-1})
2020-01-27	2458876.3638	0.552	256	11.17 ± 0.05
2020-01-28	2458876.5045	0.580	237	17.54 ± 0.06
2020-01-28	2458877.3365	0.746	223	37.70 ± 0.06
2020-01-29	2458877.5078	0.780	256	36.87 ± 0.06
2020-01-29	2458878.3251	0.943	237	11.91 ± 0.06
2020-01-30	2458878.5005	0.978	238	3.91 ± 0.06
2020-01-30	2458879.3307	0.144	277	−32.46 ± 0.05
2020-01-31	2458879.5036	0.179	255	−37.10 ± 0.06
2020-01-31	2458880.3289	0.343	232	−34.51 ± 0.06
2020-02-01	2458880.5186	0.381	191	−28.49 ± 0.06

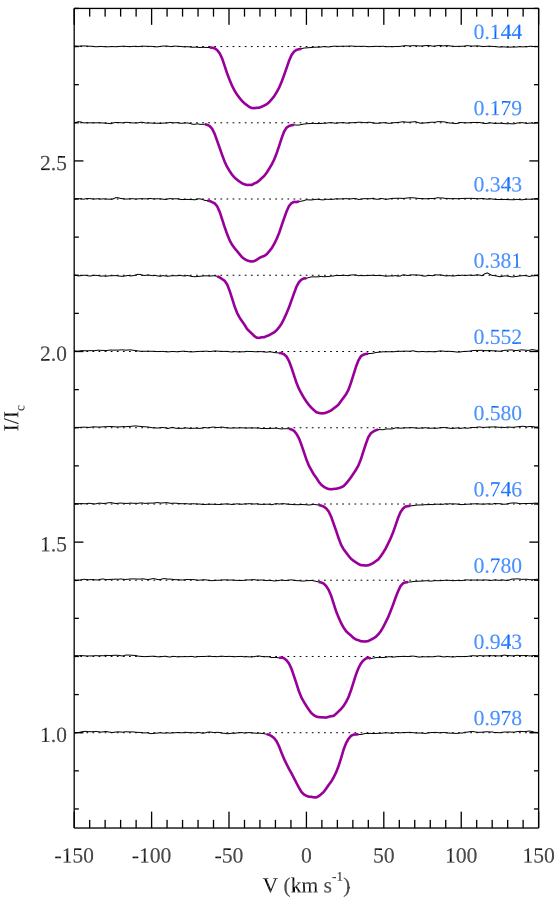

Figure 1. Least-squares deconvolved profiles of V772 Cas. Profiles for different orbital phases are shifted vertically with a step of 0.2. The dotted lines show continuum level for each spectrum. The solid lines show LSD profile for the entire velocity span with the thicker segments indicating the velocity internal employed for radial velocity measurements. The orbital phase corresponding to each observation is given on the right.

3 BINARY SYSTEM MODELLING

We subject the TESS photometry and radial velocity measurements to simultaneous modelling to determine the fundamental parameters of the components of V772 Cas. To carry out this simultaneous modelling, we wrap the PHOEBE binary modelling code (Prša & Zwitter 2005; Prsa et al. 2011) into the Markov Chain Monte Carlo (MCMC) ensemble sampling code EMCEE (Foreman-Mackey et al. 2013). This methodology has been outlined and employed in the modelling of the magnetic systems HD 66051 (Kochukhov et al. 2018) and HD 62658 (Shultz et al. 2019) and is briefly described below.

As discussed in detail by Prša & Zwitter (2005) and Prša et al. (2016), the PHOEBE code employs a generalised Roche geometry model of binary systems which treats the orbital motion of eclipsing binary-star components along with the surface brightness variation caused by limb darkening, gravity darkening, reflection, ellipsoidal variations due to non-spherical shapes of the components, and bright-

[2] Precise choice of atmospheric parameters and abundances is not important for the multi-line method used in this paper.

ness spots on their surfaces. The two latter phenomena are of particular interest here as possible explanations of the out-of-eclipse modulation observed in the TESS light curve of V772 Cas. The ellipsoidal variability arises due to the changing cross-section size that faces the observer. It occurs with the orbital period and has a distinctive shape, with two maxima and minima per orbital cycle. The minimal light corresponds to eclipse phases when the components are aligned with the line of sight. In contrast, the flux variation associated with surface spots occurs with rotational periods of the components, which are not necessarily the same as the orbital period. The shapes and amplitudes of spot-induced light curves are diverse, with the brightness extrema generally not linked to particular orbital phases. In the context of PHOEBE analysis ellipsoidal variation is an integral part of binary system modelling whereas spots are introduced with a set of additional free parameters.

3.1 Modelling setup and results

Given a set of input parameters PHOEBE produces a forward binary model that consists of both a photometric model and radial velocity model. The aim of our modelling is to obtain the input parameters which produce the PHOEBE model that best reproduces the entire observed TESS light curve, including eclipses and out-of-eclipse variation, and HERMES radial velocities. After we determine a reasonable starting model by hand, we use EMCEE to explore the posterior distributions of the free model parameters through ensemble MCMC sampling. We use 128 chains and initially run the code until it has reached 1000 iterations beyond convergence defined by a less than 1 per cent change in the estimated autocorrelation time (Foreman-Mackey et al. 2019). After convergence is reached, we record the final positions of each chain, discard all previous steps as burn-in, and re-initialize the algorithm from these points for an additional 5000 iterations. This results in 640 000 model evaluations. We marginalize over all varied parameters to arrive at posterior distributions for these parameters. From these we draw the median and 68 per cent highest posterior density confidence intervals as the parameter estimate and its 1σ uncertainty.

The TESS photometry exhibits clear eclipses with differing depths as well as out-of-eclipse variability on the orbital period. We fix the primary effective temperature according to the value derived in Sect. 4. Although the field covered by the TESS FFI surrounding the target contains numerous Gaia sources, the brightest nearby target is more than five magnitudes fainter. Following this, we assumed that the light curve of V772 Cas is not diluted by any additional light source and fixed the third light parameter to zero in our PHOEBE model.

Preliminary binary model fits with variable eccentricity indicated that this parameter does not exceed 0.02 and is statistically consistent with zero. Consequently, we fixed eccentricity in the orbit to zero in the final analysis. This can be contrasted with a marginal eccentricity of $e = 0.17 \pm 0.10$ inferred by Gandet (2008) from low-precision photographic radial velocity measurements. Since the secondary eclipse was not detected by that study, the eccentricity could not have been constrained by the light curve.

Additionally, we apply a Gaussian prior on $v_1 \sin i$, as taken from Sect. 4. For each sampled parameter combination, we calculate the corresponding component surface gravities $\log g_1$ and $\log g_2$, and use these (along with the fixed $T_{\rm eff,1}$ and sampled $T_{\rm eff,2}$) to interpolate both limb-darkening and gravity-darkening coefficients for the TESS pass-band from the tables provided by Claret (2017). For limb-darkening, we apply the square-root law. Interpolating the gravity darkening coefficients according to the effective temperatures and surface gravities of the components of a given model allows us to reduce the parameter space as opposed to varying these coefficients and checking that they are theoretically consistent *a posteriori*.

Table 2. Sampled and derived binary parameters with boundaries and estimates according to median values and uncertainties listed as 68 per cent HPD intervals.

Parameter		Prior range	HPD estimate
$P_{\rm orb}$	d	$\mathcal{U}$(0,-)	5.0138 ± 0.0001
T_0	d	$\mathcal{U}$(-,-)	2458803.4016 ± 0.0004
q	$\frac{M_2}{M_1}$	$\mathcal{U}$(0.01,1)	0.2343 ± 0.0006
a	$R_\odot$	$\mathcal{U}$(1,50)	20.60 ± 0.03
γ	km s^{-1}	$\mathcal{U}$(−50,50)	−1.6 ± 0.1
i	deg	$\mathcal{U}$(45,90)	85.40 ± 0.3
$T_{\rm eff,1}$	K	N/A	13 800
$T_{\rm eff,2}$	K	$\mathcal{U}$(3500,50000)	5750 ± 150
A_1		$\mathcal{U}$(0,1)	0.5 ± 0.3
A_2		$\mathcal{U}$(0,1)	0.4 ± 0.03
Ω_1		$\mathcal{U}$(3,20)	4.50 ± 0.03
Ω_2		$\mathcal{U}$(3,20)	6.90 ± 0.04
$\omega_{\rm rot,1}/\omega_{\rm orb}$		$\mathcal{U}$(0.1,3)	0.459 ± 0.007
l_1	per cent	$\mathcal{U}$(50,100)	99.57 ± 0.01
l_2	per cent	$\mathcal{U}$(0,50)	0.43 ± 0.01
r_1/a		N/A	0.234 ± 0.001
M_1	$M_\odot$	N/A	3.78 ± 0.02
R_1	$R_\odot$	N/A	4.83 ± 0.03
$\log g_1$	cm s^{-2}	N/A	3.648 ± 0.005
r_2/a		N/A	0.0424 ± 0.0003
M_2	$M_\odot$	N/A	0.89 ± 0.01
R_2	$R_\odot$	N/A	0.87 ± 0.01
$\log g_2$	cm s^{-2}	N/A	4.50 ± 0.01

In addition to these fixed parameters, we vary the orbital period, $P_{\rm orb}$, the reference time, T_0, the orbital inclination, i, the semi-major axis, a, the mass-ratio, q, the systemic velocity, γ, as system parameters. We also vary potentials ($\Omega_{1,2}$), albedos ($A_{1,2}$), and light contributions ($l_{1,2}$) of the primary and secondary, and vary the secondary effective temperature as well as the primary synchronicity parameter. All these parameters are allowed to vary with uniform priors, with bounds (where applicable) listed in Table 2.

Despite the lack of detection of the secondary in the spectra or LSD profiles, the presence of flat bottom secondary eclipse (which indicates a total eclipse) enables us to obtain some extra constraints on the stellar radii, and through the determination of the potentials, the mass ratio. Additionally, the presence of ellipsoidal variability provides further constraint on the mass ratio. The optimised parameter estimates and their highest posterior density (HPD) 68 per cent (1σ) uncertainties are listed in Table 2. The posterior distributions are illustrated in Figs. A1 to A4. Our solution reports an evolving intermediate mass $M_1 = 3.78 \pm 0.02\ M_\odot$, $R_1 = 4.83 \pm 0.03\ R_\odot$ primary and a lower mass $M_2 = 0.89 \pm 0.01\ M_\odot$, $R_2 = 0.87 \pm 0.01\ R_\odot$ secondary which is still in the first half of its main-sequence evolution. The size of both components is well below their Roche radii (10.8 $R_\odot$ for the primary and 5.0 $R_\odot$ for the secondary, respectively).

The optimized light curve and radial velocity models constructed

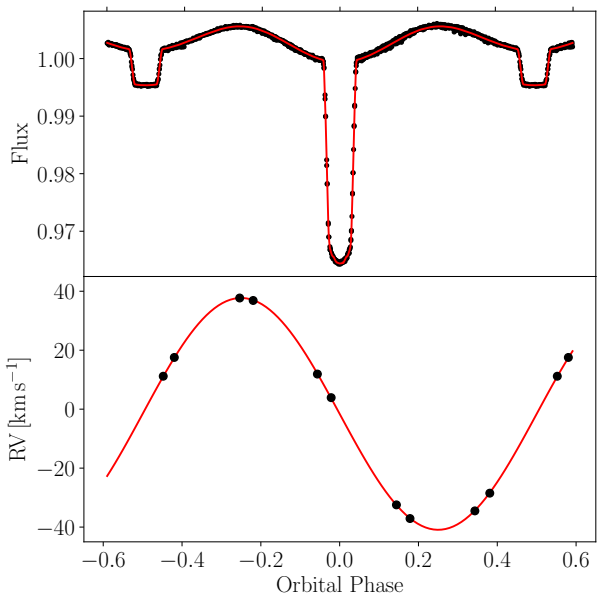

Figure 2. Top: TESS FFI observations (black symbols) and optimized PHOEBE light curve model (red line) as a function of the orbital phase. **Bottom**: Radial velocities derived from HERMES spectra (black symbols) and optimized PHOEBE radial velocity model (red line).

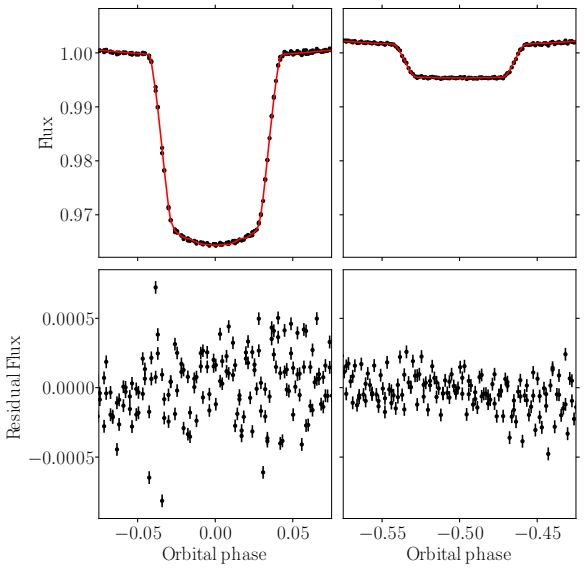

Figure 3. Top: TESS FFI observations (black symbols) and optimized PHOEBE light curve model (red line) in the vicinity of primary (left) and secondary (right) eclipses. **Bottom**: Residuals from the light curve fit.

from these parameters are shown in the top and bottom panels of Fig. 2, respectively. This figure demonstrates that the PHOEBE binary system model successfully reproduces available photometric and spectroscopic observations, both within the primary and secondary eclipses and outside the eclipses. The latter 0.6 per cent peak-to-peak photometric variation is thus interpreted as an ellipsoidal variability caused by a slightly distorted shape of the primary. Our analysis indicates that its maximum deviation from a spherical shape is about 0.7 per cent. In addition, Fig. 3 shows observations, the light curve model, and the corresponding residuals around the primary and secondary eclipses. The residuals shown in the lower panel of Fig. 3 reveal no systematic trends.

We do not include spots in our binary model as adding those would introduce several additional free parameters. There is, in fact, no evidence of spot signatures in the photometric data after ellipsoidal variation is accounted for. Inspection of the residuals after subtraction of the binary light curve model does not reveal any clear indication of rotational modulation or any other periodic variability above $\approx$ 100 ppm for the frequencies below 2 d^{-1} and 20 ppm in the 2–24 d^{-1} frequency range.

Given the sharp points of ingress and egress (the first and fourth contacts) at both primary and secondary eclipse, we ran two PHOEBE models with different fine and coarse grid sizes to characterise the numerical noise in our solution. We find a difference of 18 ppm between the two models, whereas the residual scatter is 230 ppm, meaning that the numerical noise is responsible for less than 10 per cent of the residual scatter (Maxted et al. 2020).

4 ANALYSIS OF HGMN PRIMARY

4.1 Atmospheric parameters

Here we use a combination of modelling the stellar spectral energy distribution (SED) and the hydrogen Balmer lines to determine primary's $T_{\rm eff}$ and $\log g$ respectively. This approach is commonly employed for normal and peculiar late-B and A-type stars (e.g. Ryabchikova, Malanushenko & Adelman 1999; Fossati et al. 2009; Rusomarov et al. 2016; Kochukhov, Shultz & Neiner 2019). Other spectral indicators, such as He I and metal lines, cannot be used for the atmospheric parameter determination of HgMn stars due to non-solar photospheric element abundances and occasional vertical chemical stratification.

Model atmosphere analysis of the primary component of V772 Cas was carried out using the LLmodels code (Shulyak et al. 2004), taking into account individual atmospheric abundances. The influence of the faint secondary was ignored. The effective temperature was determined by comparing the model SED with the TD1 satellite stellar flux measurements in UV (Thompson et al. 1978) as well as the optical and near-infrared fluxes obtained from Geneva (Hauck & North 1982) and 2MASS (Cutri et al. 2003) photometric measurements, respectively. The reddening $E(B-V) = 0.144 \pm 0.050$ (Lallement et al. 2019) and the Gaia DR2 distance 363 ± 6 pc (Gaia Collaboration et al. 2018) were adopted for SED fitting with the stellar effective temperature and radius adjusted to match the observations. This analysis yielded $T_{\rm eff} = 13800 \pm 500$ K and $R = 4.95 \pm 0.2\ R_\odot$. Figure 4 compares observations with the theoretical SED computed with LLmodels using these parameters. The stellar effective temperature derived from the SED agrees reasonably well with $T_{\rm eff} = 13400$–13800 K that can be obtained for this star using different Strömgren and Geneva photometric calibrations (Kunzli et al. 1997; Paunzen, Schnell & Maitzen 2005; Paunzen, Schnell & Maitzen 2006).

The surface gravity was determined by fitting the observed hydrogen Balmer line profiles in the time-averaged HERMES spectrum with the theoretical calculations using the Synth3 spectrum synthesis code (Kochukhov 2007) and the LLmodels atmospheres described above. The average spectrum was constructed by co-adding ten individual observations after correcting the radial velocity shifts reported in Table 1. As demonstrated by Fig. 5, the hydrogen lines in the mean spectrum of the primary are well approximated with

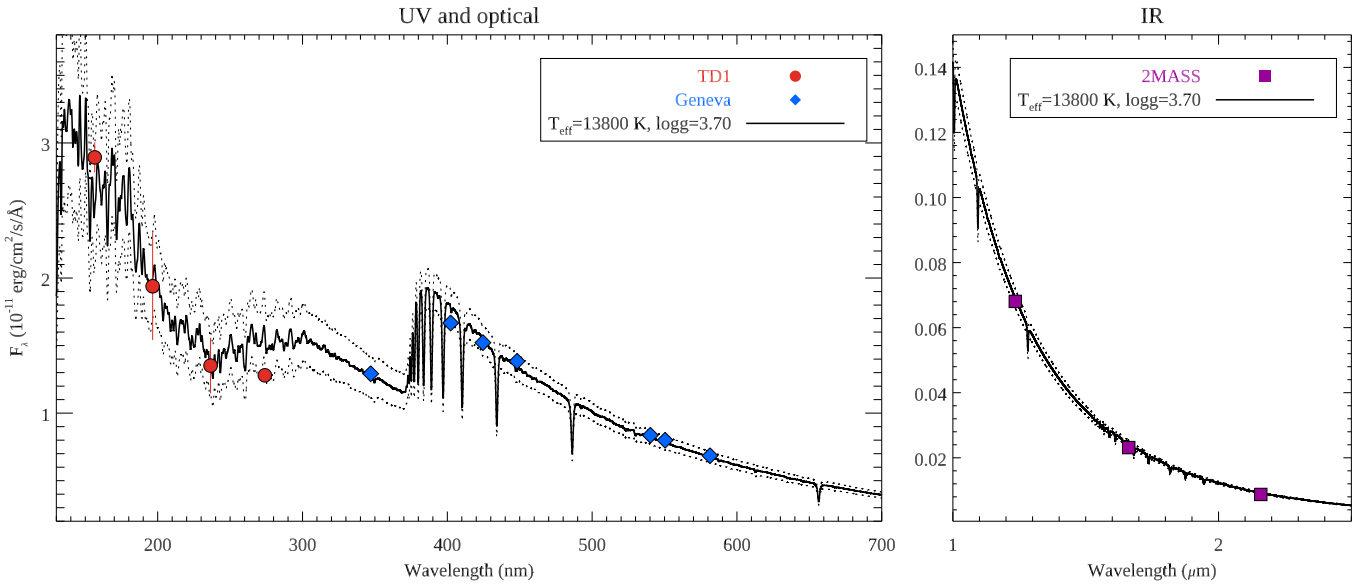

Figure 4. Comparison between the observed (symbols) and theoretical (lines) spectral energy distribution of V772 Cas in the ultraviolet and optical (left panel) and near-infrared (right panel) wavelength regions. Calculation shown with the thick solid line corresponds to primary's parameters $T_{\rm eff} = 13800$ K, $\log g = 3.7$, $R = 4.95\,R_\odot$, and reddening $E(B-V) = 0.144$. Dotted lines illustrate the impact of changing $T_{\rm eff}$ by ±500 K.

$\log g = 3.7 \pm 0.1$. This spectroscopic estimate of $\log g$ and the stellar radius inferred from the SED are consistent within uncertainty with the results of binary system modelling with PHOEBE in Sect. 3.1.

4.2 Abundances

Chemical abundances were estimated by fitting Synth3 spectra to short segments of the average spectrum of V772 Cas. In these fits, individual abundances of one or several elements as well as the projected rotational velocity were determined using the BinMag (Kochukhov 2018)[3] IDL tool. Different lines of the same ions were analysed independently and the scatter of abundances, quantified by the standard deviation, was taken as an uncertainty estimate. The input line list for these calculations was extracted from VALD, using the latest version of the database that incorporates hyperfine and isotopic splitting (Pakhomov et al. 2019). For V772 Cas the former is particularly important for accurate analysis of Mn II and Ga II lines. Information on the hyperfine and isotopic splitting of the Hg II 3984 Å line was taken from Woolf & Lambert (1999).

Several examples of spectrum synthesis fits around the lines typically enhanced in HgMn stars are shown in Fig. 6. Examples of fits to other ions analysed in the paper are demonstrated in Fig. B1. We were able to obtain abundance estimates for 19 ions based on 164 individual lines and blends, listed in Table B1. The resulting abundances are presented in Table 3, which lists the ions studied, the number of lines analysed, the average abundance and corresponding error for V772 Cas, the corresponding average abundance of HgMn stars with $T_{\rm eff} = 13000$–14000 K from the compilation by Ghazaryan et al. (2018), and the solar abundance of each ion (Asplund et al. 2009). Our abundance analysis of V772 Cas was carried out under the local thermodynamic equilibrium (LTE) assumption. Several abundances reported in Table 3, for example Ca (Sitnova, Mashonkina & Ryabchikova 2018), Si (Mashonkina 2020), and Ne (Alexeeva et al. 2020), are likely affected by departures from LTE leading to abundance corrections of about 0.1–0.3 dex.

The abundance pattern of V772 Cas relative to the solar chemical composition is illustrated in Fig. 7. We also show in this figure abundances of 33 HgMn stars in the 13000–14000 K $T_{\rm eff}$ range from the catalogue by Ghazaryan et al. (2018). It is evident that V772 Cas exhibits an unremarkable abundance pattern, very often seen in HgMn stars with a similar $T_{\rm eff}$. In particular, He is underabundant, Si is close to solar, P and Mn are overabundant by ~ 2 dex, and Ga, Xe, and Hg are overabundant by up to 4 dex. Pr is also overabundant in V772 Cas by ≈ 2.5 dex, as found for several other HgMn stars, although its abundance estimate based on a single blended Pr III line is somewhat uncertain.

Considering the projected rotational velocity, determined with the spectrum synthesis fit from 84 unblended lines, we found $v_{\rm e} \sin i = 22.3 \pm 0.3$ km s^{-1}. Together with the stellar radius $R = 4.83 \pm 0.03\,R_\odot$ and inclination of the rotation axis $i_{\rm rot} = i_{\rm orb} = 85.4 \pm 0.3^\circ$ found in Sect. 3, this implies $P_{\rm rot} = 10.9 \pm 0.2$ d. Thus, the primary is rotating sub-synchronously with a period about twice longer than the orbital period provided that the orbital and rotational axes are aligned. The latter assumption is reasonable for close binaries on theoretical grounds (Zahn 1977; Hut 1981) and generally agrees with observational findings (Hale 1994; Farbiash & Steinitz 2004).

5 DISCUSSION

In this paper we investigated the nature of the bright but poorly studied eclipsing binary system V772 Cas. Based on the new high-precision photometric data provided by the TESS mission we confirmed the presence of primary eclipses and identified secondary eclipses for the first time. Significant out-of-eclipse photometric variability, synchronised with the orbital motion, was confirmed for this system. We have acquired high-resolution spectra of V772 Cas with the aim to determine fundamental parameters of the components and better

[3] https://www.astro.uu.se/~oleg/binmag.html

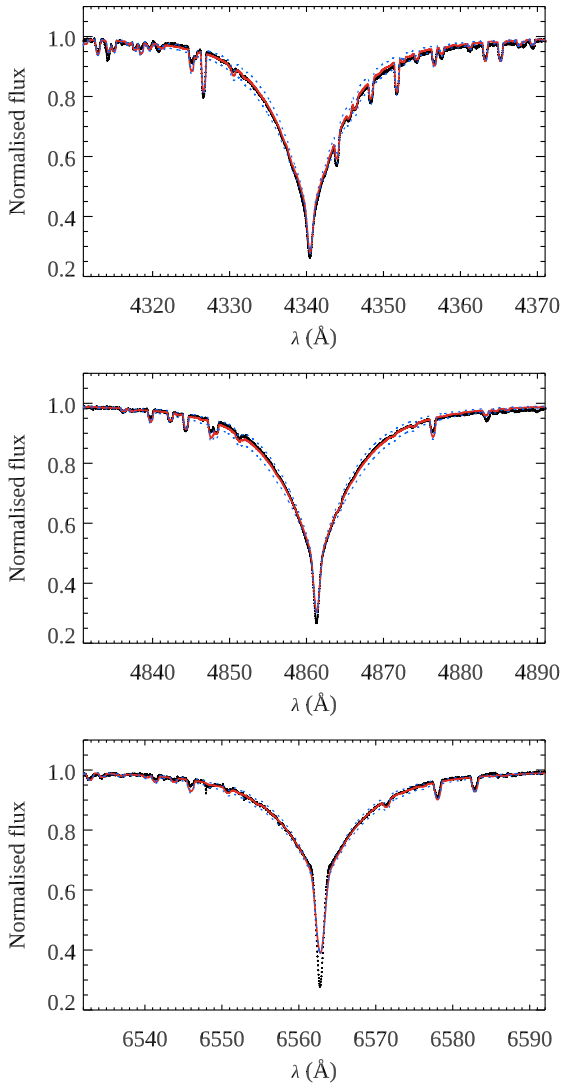

Figure 5. Comparison between the observed (symbols) and theoretical (lines) hydrogen Balmer line profiles. Calculations shown with solid lines employ $T_{\rm eff} = 13800$ K, $\log g = 3.7$ model atmosphere for the primary together with the chemical abundances determined in this study. Dotted lines illustrate the effect of changing $\log g$ by ±0.2 dex.

characterise surface abundance pattern of the primary star, which in the past was attributed conflicting HgMn and BpSi spectral classifications.

Our analysis reveals that V772 Cas is an SB1 system with a late-B primary showing abundance anomalies typical of HgMn stars. Measurement of the projected rotational velocity shows that the primary rotates sub-synchronously. Taking into account constraints from the atmospheric modelling of the primary, we carried out detailed modelling of the TESS light curve with the PHOEBE code. This analysis demonstrated that the conspicuous out-of-eclipse variability is explained by the ellipsoidal shape of the primary, which arises due to the tidal interaction with the secondary. The ellipsoidal variability is clearly visible in the TESS light curve despite a relatively low mass of the secondary thanks to a high precision of the space photometry data. Interpretation of the ellipsoidal variability together with eclipses and radial velocity variation of the primary allowed us to retrieve accurate masses and radii of both components despite the absence of the secondary's lines in the optical spectra. We concluded

Table 3. Atmospheric chemical composition of the primary component of V772 Cas. The columns give the ion identification, the number of lines studied, abundance for V772 Cas, average abundance for HgMn stars in the 13000–14000 $T_{\rm eff}$ interval (Ghazaryan et al. 2018), and the solar abundance (Asplund et al. 2009).

Ion	N	$\log(N_{\rm el}/N_{\rm tot})$		
		V772 Cas	⟨HgMn⟩	Sun
He I	5	−2.02 ± 0.10	−2.01 ± 0.52	−1.11
C II	3	−3.80 ± 0.15	−4.05 ± 0.48	−3.61
O I	2	−3.37 ± 0.16	−3.36 ± 0.13	−3.35
Ne I	11	−3.63 ± 0.04	−4.29 ± 0.47	−4.11
Mg II	3	−4.73 ± 0.14	−5.16 ± 0.53	−4.44
Si II	5	−4.38 ± 0.09	−4.89 ± 0.63	−4.53
Si III	2	−4.56 ± 0.01	−4.89 ± 0.63	−4.53
P II	21	−4.63 ± 0.22	−4.94 ± 0.48	−6.63
S II	8	−5.89 ± 0.10	−5.28 ± 0.63	−4.92
Ca II	1	−5.10	−5.32 ± 0.41	−5.70
Ti II	8	−6.10 ± 0.07	−6.58 ± 0.36	−7.09
Cr II	6	−5.68 ± 0.06	−6.24 ± 0.51	−6.40
Mn II	38	−4.17 ± 0.14	−4.97 ± 0.86	−6.61
Fe II	42	−4.11 ± 0.10	−4.32 ± 0.50	−4.54
Ni II	1	−5.91	−6.20 ± 0.43	−5.82
Ga II	3	−5.42 ± 0.20	−5.87 ± 1.13	−9.00
Xe II	3	−5.37 ± 0.35	−5.51 ± 0.58	−9.80
Pr III	1	−8.66:	−9.21 ± 1.10	−11.32
Hg II	1	−6.81	−6.49 ± 1.09	−10.87

that an evolved HgMn primary of V772 Cas is orbited by a main sequence solar-type secondary, resulting in large luminosity and mass ratios.

Our results confirm that V772 Cas should be formally classified as an Algol-type (EA) eclipsing binary (Samus' et al. 2017), without any additional types of variability present. In particular, the absence of rotational modulation due to surface spots and the HgMn spectroscopic classification of the primary demonstrates that this star is not an α^2 CVn-type magnetic variable similar to the magnetic Bp stars recently identified in the eclipsing binaries HD 66051 (Kochukhov et al. 2018) and HD 65658 (Shultz et al. 2019). Instead, V772 Cas should be discussed in the context of research on HgMn stars. These objects lack strong large-scale magnetic fields (Shorlin et al. 2002; Aurière et al. 2010; Bagnulo et al. 2012; Kochukhov et al. 2011; Makaganiuk et al. 2011a,b, 2012) and also possess no complex tangled fields stronger than a few hundred G (Kochukhov et al. 2013). Despite this, these stars are able to develop a low-contrast non-uniform surface abundance distribution of some heavy elements (Adelman et al. 2002; Kochukhov 2005; Folsom et al. 2010; Makaganiuk et al. 2011b). Geometry of these abundance spots appears to slowly evolve with time (Kochukhov et al. 2007; Briquet et al. 2010; Korhonen et al. 2013). Photometric time series studies of HgMn stars occasionally reveal rotational modulation, presumably related to heavy-element abundance spots (Morel et al. 2014; Strassmeier et al. 2017; White et al. 2017; Prvák, Krtička & Korhonen 2020), and, possibly, to SPB pulsations (Hümmerich et al. 2018). Our study shows that ellipsoidal variability is yet another phenomenon that can contribute to or even dominate the light curves of HgMn stars in close binaries.

Although HgMn stars are commonly found in close binary systems (Abt & Snowden 1973; Gerbaldi et al. 1985), only two eclipsing binaries containing HgMn components were known prior to this study. They are AR Aur (Nordstrom & Johansen 1994; Folsom et al. 2010; Hubrig et al. 2012) and TYC 455-791-1 (Strassmeier et al. 2017). Table 4 summarises the properties of these three systems in compar-

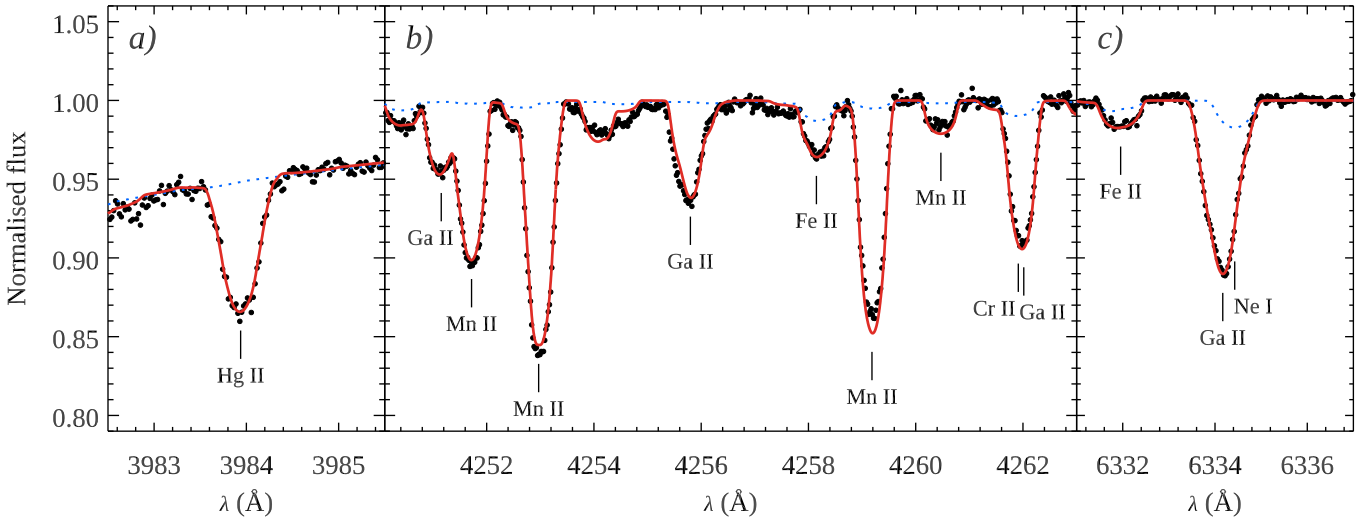

Figure 6. Comparison of the average spectrum of V772 Cas (symbols) with the best fitting theoretical model spectrum (solid line) in several wavelength regions containing spectral lines commonly enhanced in HgMn stars. Dotted line shows synthetic spectrum calculated with solar abundances.

Table 4. Properties of eclipsing binary systems containing HgMn stars. When available, uncertainties in the last significant digit are indicated by the numbers in brackets.

Star	V	Spec	$P_{\rm orb}$ (d)	e	q	M_1 ($M_\odot$)	R_1 ($R_\odot$)	M_2 ($M_\odot$)	R_2 ($R_\odot$)	Reference
AR Aur	6.14	SB2	4.13	0.0	0.927(2)	2.544(9)	1.80(1)	2.358(8)	1.83(2)	Hubrig et al. (2012)
TYC 455-791-1	11.95	SB2	12.47	0.18	0.941(8)	3.1	2.4	2.9	2.3	Strassmeier et al. (2017)
V772 Cas	6.68	SB1	5.01	0.0	0.2343(6)	3.78(2)	4.83(3)	0.89(1)	0.87(1)	This work

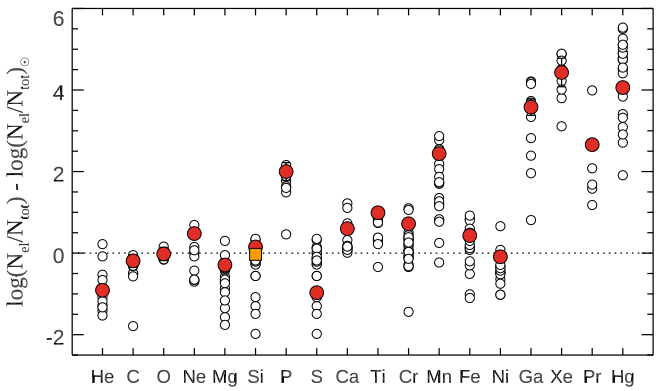

Figure 7. Abundances of individual elements in the primary component of V772 Cas (filled symbols) relative to the solar chemical composition. Filled circles correspond to neutral and singly ionised species; the filled square shows the abundance of Si III. Open symbols illustrate abundances of HgMn stars with $T_{\rm eff}$ = 13000–14000 K from the catalogue by Ghazaryan et al. (2018).

ison to V772 Cas. All three eclipsing binaries are non-interacting, detached systems, so their components should have evolved as if they were single stars (Torres, Andersen & Giménez 2010). The resulting mass-radius relationship is compared to single-star MESA (Modules for Experiments in Stellar Astrophysics) theoretical stellar evolution models from the MIST grid[4] (Dotter 2016; Choi et al. 2016) in Fig. 8. These models are available for two values of initial rotational velocity, a wide metallicity range, and a single empirically calibrated overshooting prescription, consistent with recent observational constraints (Claret & Torres 2019). In this work, we have chosen to use the isochrones that were computed ignoring the stellar rotation. This assumption is appropriate for the three systems considered here and for HgMn stars in general since a slow rotation is known to be a necessary condition for this chemical peculiarity to appear (Michaud 1982).

The chemical anomalies produced by the atomic diffusion in A and B stars are constrained to the outermost stellar layers and are not indicative of the bulk metallicity (e.g. Richard, Michaud & Richer 2001). The latter is unknown but is believed to not differ much from that of normal stars. According to Sofia & Meyer (2001), the metallicity scatter of young F and G disk stars in the solar neighbourhood reaches 0.1–0.2 dex, which is similar to the 0.4 dex metallicity range of open clusters containing ApBp stars (Bagnulo et al. 2006; Landstreet et al. 2007). Therefore, we included a metallicity variation by ±0.2 dex around the solar value when estimating the age of V772 Cas from the MIST isochrones.

In all three systems the star with HgMn peculiarity is the primary. AR Aur and TYC 455-791-1 are close to ZAMS and have mass ratios not far from unity. In fact, AR Aur B is probably still contracting towards ZAMS, indicating the extreme youth of this system (Nordstrom & Johansen 1994). The masses of the components of AR Aur and TYC 455-791-1 span a narrow range of 2.4–3.1 $M_\odot$.

[4] http://waps.cfa.harvard.edu/MIST

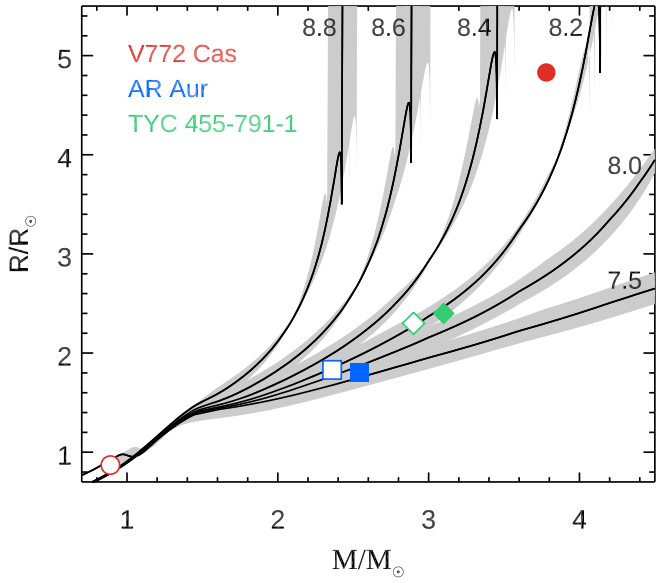

Figure 8. Masses and radii of the eclipsing binaries with HgMn components. Parameters of the primaries are indicated by filled symbols. Open symbols correspond to the secondaries. The three systems included in this plot are V772 Cas (circles), AR Aur (squares), and TYC 455-791-1 (diamonds). Theoretical MESA isochrones corresponding to ages from $\log t/\mathrm{yr} = 7.5$ to 8.8 are also shown. The underlying grey curves illustrate the effect of varying metallicity by ±0.2 dex.

On the other hand, the primary of V772 Cas is more massive and considerably more evolved. It is likely to be at or near the TAMS whereas the solar-type secondary is still on the main sequence. The location of V772 Cas components on the mass-radius diagram illustrated in Fig. 8 is best described by a set of isochrones with ages from $\log t/\mathrm{yr} = 8.26$ to 8.32 for the metallicity range discussed above and the standard overshooting prescription adopted in the MIST grid. A similar age range (8.32–8.38) is obtained by applying the isochrone-cloud fitting methodology (Johnston et al. 2019) with a different grid of solar-metallicity MESA models spanning a large range of overshooting parameter.

Despite this dramatic difference in evolutionary status, the HgMn primaries of all three eclipsing binary systems share the same basic chemical abundance pattern. This observation suggests that the HgMn-type chemical peculiarity develops rapidly at or near the ZAMS and then persists throughout the entire main sequence life time of an intermediate-mass star. This is broadly in agreement with the investigation of H-R diagram positions of single HgMn stars by Adelman, Adelman & Pintado (2003), although that study showed that these stars tend to concentrate in the first half of the main-sequence life time and that there are very few luminous HgMn stars comparable to V772 Cas A.

ACKNOWLEDGEMENTS

Based on observations made with the Mercator Telescope, operated on the Island of La Palma by the Flemish Community, at the Spanish Observatorio del Roque de los Muchachos of the Instituto de Astrofísica de Canarias. This work has made use of the VALD database, operated at Uppsala University, the Institute of Astronomy RAS in Moscow, and the University of Vienna. This research has made use of the SIMBAD database, operated at CDS, Strasbourg, France. Some of the data presented in this paper were obtained from the Mikulski Archive for Space Telescopes (MAST). O.K. acknowledges support by the Swedish Research Council and the Swedish National Space Board. J.L.-B. acknowledges support from FAPESP (grant 2017/23731-1). This paper includes data collected by the TESS mission, which are publicly available from the Mikulski Archive for Space Telescopes (MAST). Funding for the TESS mission is provided by NASA's Science Mission directorate. This research made use of Astropy,[5] a community-developed core Python package for Astronomy (Astropy Collaboration et al. 2013, 2018) as well as the Corner[6] Python code by Foreman-Mackey (2016). The research leading to these results has received funding from the European Research Council (ERC) under the European Union's Horizon 2020 research and innovation programme (grant agreement N°670519: MAMSIE), from the KU Leuven Research Council (grant C16/18/005: PARADISE), from the Research Foundation Flanders (FWO) under grant agreements G0H5416N (ERC Runner Up Project) and G0A2917N (BlackGEM), as well as from the BELgian federal Science Policy Office (BELSPO) through PRODEX grant PLATO. T.R. thanks the Ministry of Science and Higher Education of Russian Federation (grant 13.1902.21.0039) for partial financial support. M.E.S. acknowledges support from the Annie Jump Cannon Fellowship, supported by the University of Delaware and endowed by the Mount Cuba Astronomical Observatory.

DATA AVAILABILITY

The data underlying this article will be shared on reasonable request to the corresponding author.

REFERENCES

Abt H. A., Snowden M. S., 1973, ApJS, 25, 137
Adelman S. J., Gulliver A. F., Kochukhov O. P., Ryabchikova T. A., 2002, ApJ, 575, 449
Adelman S. J., Adelman A. S., Pintado O. I., 2003, A&A, 397, 267
Alecian E., et al., 2015, in Meynet G., Georgy C., Groh J., Stee P., eds, IAU Symposium Vol. 307, New Windows on Massive Stars. pp 330–335
Alexeeva S., Chen T., Ryabchikova T., Shi W., Sadakane K., Nishimura M., Zhao G., 2020, ApJ, 896, 59
Asplund M., Grevesse N., Sauval A. J., Scott P., 2009, ARA&A, 47, 481
Astropy Collaboration et al., 2013, A&A, 558, A33
Astropy Collaboration et al., 2018, AJ, 156, 123
Aurière M., et al., 2007, A&A, 475, 1053
Aurière M., et al., 2010, A&A, 523, A40
Bagnulo S., Landstreet J. D., Mason E., Andretta V., Silaj J., Wade G. A., 2006, A&A, 450, 777
Bagnulo S., Landstreet J. D., Fossati L., Kochukhov O., 2012, A&A, 538, A129
Braithwaite J., Spruit H. C., 2004, Nature, 431, 819
Brasseur C. E., Phillip C., Fleming S. W., Mullally S. E., White R. L., 2019, Astrocut: Tools for creating cutouts of TESS images (ascl:1905.007)
Briquet M., Korhonen H., González J. F., Hubrig S., Hackman T., 2010, A&A, 511, A71
Carquillat J. M., Prieur J. L., 2007, MNRAS, 380, 1064
Choi J., Dotter A., Conroy C., Cantiello M., Paxton B., Johnson B. D., 2016, ApJ, 823, 102
Claret A., 2017, A&A, 600, A30
Claret A., Torres G., 2019, ApJ, 876, 134

[5] http://www.astropy.org
[6] https://corner.readthedocs.io

Cowley A., 1972, AJ, 77, 750
Cutri R. M., et al., 2003, VizieR Online Data Catalog, p. II/246
Dotter A., 2016, ApJS, 222, 8
Dworetsky M. M., 1976, in Weiss W. W., Jenkner H., Wood H. J., eds, IAU Colloq. 32: Physics of Ap Stars. p. 549
Farbiash N., Steinitz R., 2004, in Allen C., Scarfe C., eds, Revista Mexicana de Astronomia y Astrofisica Conference Series Vol. 21, Revista Mexicana de Astronomia y Astrofisica Conference Series. pp 15–19
Folsom C. P., Kochukhov O., Wade G. A., Silvester J., Bagnulo S., 2010, MNRAS, 407, 2383
Foreman-Mackey D., 2016, The Journal of Open Source Software, 1, 24
Foreman-Mackey D., Hogg D. W., Lang D., Goodman J., 2013, PASP, 125, 306
Foreman-Mackey D., et al., 2019, The Journal of Open Source Software, 4, 1864
Fossati L., Ryabchikova T., Bagnulo S., Alecian E., Grunhut J., Kochukhov O., Wade G., 2009, A&A, 503, 945
Gaia Collaboration et al., 2018, A&A, 616, A1
Gandet T. L., 2008, Information Bulletin on Variable Stars, 5848, 1
Gerbaldi M., Floquet M., Hauck B., 1985, A&A, 146, 341
Ghazaryan S., Alecian G., Hakobyan A. A., 2018, MNRAS, 480, 2953
González J. F., Hubrig S., Castelli F., 2010, MNRAS, 402, 2539
Hale A., 1994, AJ, 107, 306
Hauck B., North P., 1982, A&A, 114, 23
Hensberge H., et al., 2007, MNRAS, 379, 349
Huang W., Gies D. R., McSwain M. V., 2010, ApJ, 722, 605
Hube D. P., 1970, Mem. RAS, 72, 233
Hubrig S., et al., 2012, A&A, 547, A90
Hümmerich S., Niemczura E., Walczak P., Paunzen E., Bernhard K., Murphy S. J., Drobek D., 2018, MNRAS, 474, 2467
Hut P., 1981, A&A, 99, 126
Johnston C., Tkachenko A., Aerts C., Molenberghs G., Bowman D. M., Pedersen M. G., Buysschaert B., Pápics P. I., 2019, MNRAS, 482, 1231
Kazarovets E. V., Samus N. N., Durlevich O. V., Frolov M. S., Antipin S. V., Kireeva N. N., Pastukhova E. N., 1999, Information Bulletin on Variable Stars, 4659, 1
Kochukhov O., 2005, A&A, 438, 219
Kochukhov O., 2007, in Romanyuk I. I., Kudryavtsev D. O., eds, Physics of Magnetic Stars. pp 109–118
Kochukhov O., 2018, BinMag: Widget for comparing stellar observed with theoretical spectra, Astrophysics Source Code Library (ascl:1805.015)
Kochukhov O., Adelman S. J., Gulliver A. F., Piskunov N., 2007, Nature Physics, 3, 526
Kochukhov O., Makaganiuk V., Piskunov N., 2010, A&A, 524, A5
Kochukhov O., et al., 2011, A&A, 534, L13
Kochukhov O., et al., 2013, A&A, 554, A61
Kochukhov O., Johnston C., Alecian E., Wade G. A., 2018, MNRAS, 478, 1749
Kochukhov O., Shultz M., Neiner C., 2019, A&A, 621, A47
Korhonen H., et al., 2013, A&A, 553, A27
Kunzli M., North P., Kurucz R. L., Nicolet B., 1997, A&AS, 122, 51
Lallement R., Babusiaux C., Vergely J. L., Katz D., Arenou F., Valette B., Hottier C., Capitanio L., 2019, A&A, 625, A135
Landstreet J. D., Bagnulo S., Andretta V., Fossati L., Mason E., Silaj J., Wade G. A., 2007, A&A, 470, 685
Landstreet J. D., Kochukhov O., Alecian E., Bailey J. D., Mathis S., Neiner C., Wade G. A., BINaMIcS Collaboration 2017, A&A, 601, A129
Lightkurve Collaboration et al., 2018, Lightkurve: Kepler and TESS time series analysis in Python, Astrophysics Source Code Library (ascl:1812.013)
Makaganiuk V., et al., 2011a, A&A, 525, A97
Makaganiuk V., et al., 2011b, A&A, 529, A160
Makaganiuk V., et al., 2012, A&A, 539, A142
Mashonkina L., 2020, MNRAS, 493, 6095
Mathys G., 2017, A&A, 601, A14
Maxted P. F. L., et al., 2020, MNRAS,
Mestel L., 1999, Stellar magnetism. Oxford Science Publications
Michaud G., 1982, ApJ, 258, 349
Michaud G., Alecian G., Richer J., 2015, Atomic Diffusion in Stars, doi:10.1007/978-3-319-19854-5.
Morel T., et al., 2014, A&A, 561, A35
Moss D., 2004, in Zverko J., Ziznovsky J., Adelman S. J., Weiss W. W., eds, IAU Symposium Vol. 224, The A-Star Puzzle. pp 245–252
Neiner C., Mathis S., Alecian E., Emeriau C., Grunhut J., BinaMIcS MiMeS Collaborations 2015, in Nagendra K. N., Bagnulo S., Centeno R., Jesús Martínez González M., eds, IAU Symposium Vol. 305, Polarimetry. pp 61–66
Nordstrom B., Johansen K. T., 1994, A&A, 282, 787
Otero S. A., 2007, Open European Journal on Variable Stars, 0072, 1
Pakhomov Y. V., Ryabchikova T. A., Piskunov N. E., 2019, Astronomy Reports, 63, 1010
Paunzen E., Schnell A., Maitzen H. M., 2005, A&A, 444, 941
Paunzen E., Schnell A., Maitzen H. M., 2006, A&A, 458, 293
Perryman M. A. C., et al., 1997, A&A, 323, L49
Prsa A., Matijevic G., Latkovic O., Vilardell F., Wils P., 2011, PHOEBE: PHysics Of Eclipsing BinariEs, Astrophysics Source Code Library (ascl:1106.002)
Prša A., Zwitter T., 2005, ApJ, 628, 426
Prša A., et al., 2016, ApJS, 227, 29
Prvák M., Krtička J., Korhonen H., 2020, MNRAS, 492, 1834
Raskin G., et al., 2011, A&A, 526, A69
Renson P., Manfroid J., 2009, A&A, 498, 961
Richard O., Michaud G., Richer J., 2001, ApJ, 558, 377
Ricker G. R., et al., 2015, Journal of Astronomical Telescopes, Instruments, and Systems, 1, 014003
Rosén L., Kochukhov O., Alecian E., Neiner C., Morin J., Wade G. A., BinaMIcS Collaboration 2018, A&A, 613, A60
Rusomarov N., Kochukhov O., Ryabchikova T., Ilyin I., 2016, A&A, 588, A138
Ryabchikova T., 1998, Contributions of the Astronomical Observatory Skalnate Pleso, 27, 319
Ryabchikova T. A., Malanushenko V. P., Adelman S. J., 1999, A&A, 351, 963
Ryabchikova T., Piskunov N., Kurucz R. L., Stempels H. C., Heiter U., Pakhomov Y., Barklem P. S., 2015, Phys. Scr., 90, 054005
Samus' N. N., Kazarovets E. V., Durlevich O. V., Kireeva N. N., Pastukhova E. N., 2017, Astronomy Reports, 61, 80
Schneider F. R. N., Podsiadlowski P., Langer N., Castro N., Fossati L., 2016, MNRAS, 457, 2355
Schneider F. R. N., Ohlmann S. T., Podsiadlowski P., Röpke F. K., Balbus S. A., Pakmor R., Springel V., 2019, Nature, 574, 211
Shorlin S. L. S., Wade G. A., Donati J.-F., Landstreet J. D., Petit P., Sigut T. A. A., Strasser S., 2002, A&A, 392, 637
Shultz M. E., et al., 2019, MNRAS, 490, 4154
Shulyak D., Tsymbal V., Ryabchikova T., Stütz C., Weiss W. W., 2004, A&A, 428, 993
Sikora J., Wade G. A., Power J., Neiner C., 2019, MNRAS, 483, 3127
Sitnova T. M., Mashonkina L. I., Ryabchikova T. A., 2018, MNRAS, 477, 3343
Skarka M., et al., 2019, MNRAS, 487, 4230
Sofia U. J., Meyer D. M., 2001, ApJ, 554, L221
Strassmeier K. G., Granzer T., Mallonn M., Weber M., Weingrill J., 2017, A&A, 597, A55
Takeda Y., Han I., Kang D.-I., Lee B.-C., Kim K.-M., 2019, MNRAS, 485, 1067
Thompson G. I., Nandy K., Jamar C., Monfils A., Houziaux L., Carnochan D. J., Wilson R., 1978, Catalogue of stellar ultraviolet fluxes : a compilation of absolute stellar fluxes measured by the Sky Survey Telescope (S2/68) aboard the ESRO satellite TD-1
Torres G., Andersen J., Giménez A., 2010, A&ARv, 18, 67
Vidotto A. A., et al., 2014, MNRAS, 441, 2361
White T. R., et al., 2017, MNRAS, 471, 2882
Woolf V. M., Lambert D. L., 1999, ApJ, 521, 414
Zahn J.-P., 1977, A&A, 57, 383
de Mink S. E., Sana H., Langer N., Izzard R. G., Schneider F. R. N., 2014, ApJ, 782, 7

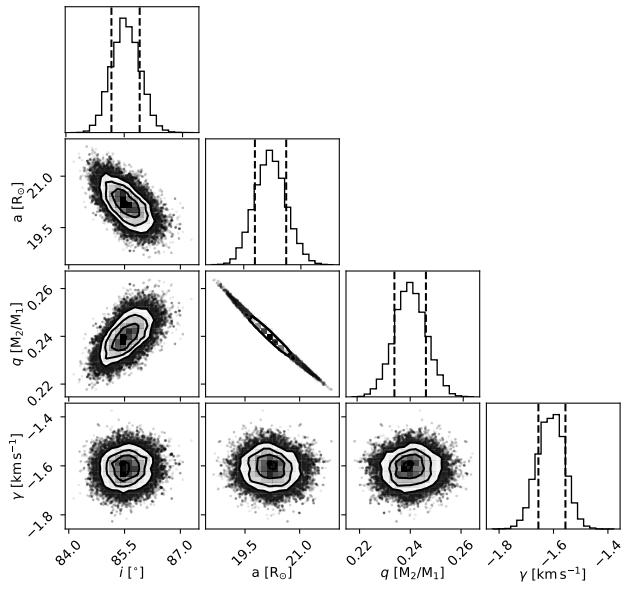

Figure A1. Marginalised posterior distributions for orbital parameters. The dashed lines in histogram plots denote 68 per cent (1σ) confidence ranges. The contours in the probability density plots correspond to 0.5, 1.0, 1.5, and 2.0σ confidence intervals.

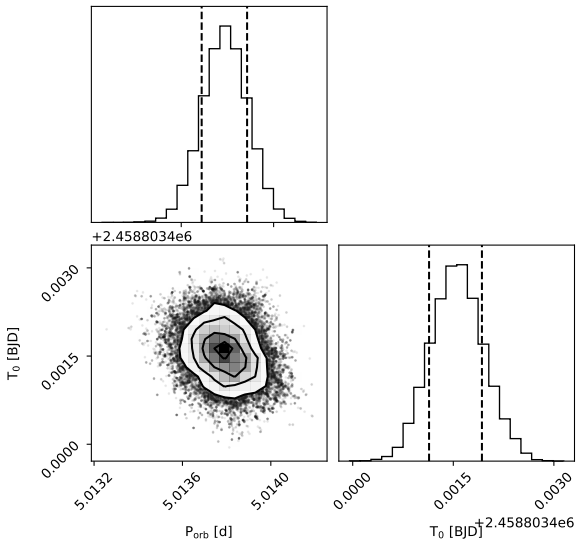

Figure A2. Same as Fig. A1, but for the orbital ephemeris.

APPENDIX A: POSTERIOR PROBABILITY DISTRIBUTIONS

APPENDIX B: SPECTRUM SYNTHESIS FITS AND LIST OF LINES EMPLOYED FOR ABUNDANCE DETERMINATION

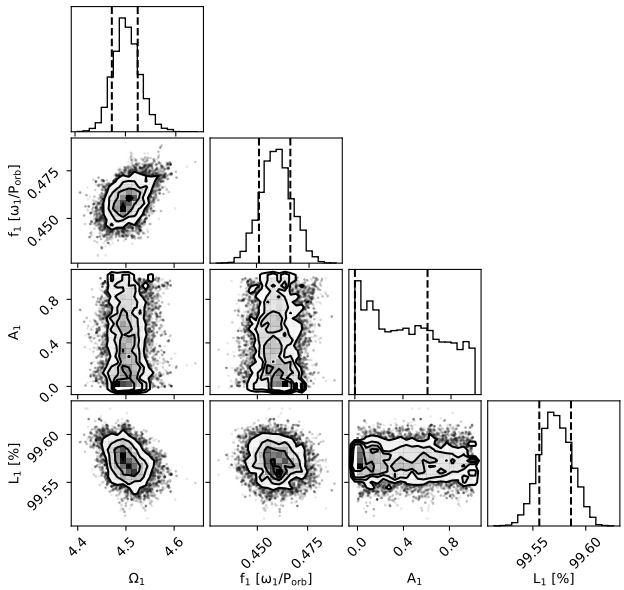

Figure A3. Same as Fig. A1, but for the parameters of the primary star.

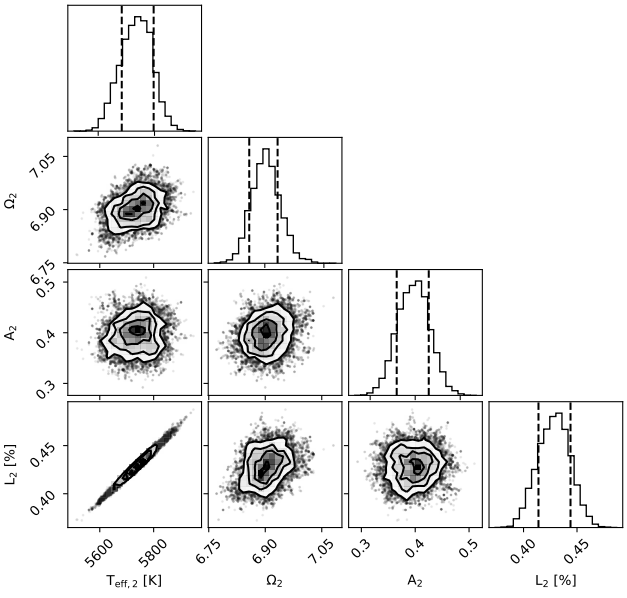

Figure A4. Same as Fig. A1, but for the parameters of the secondary star.

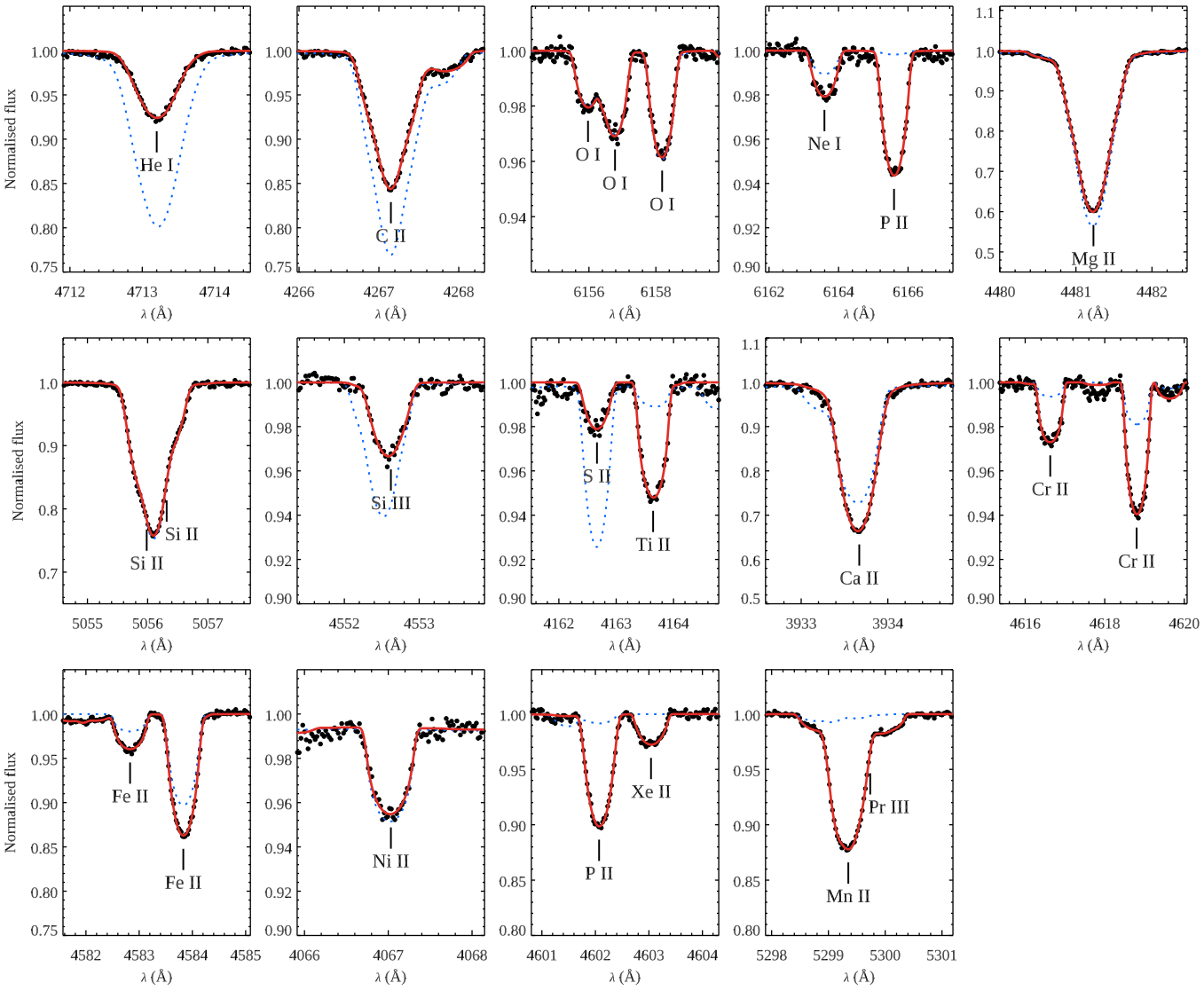

Figure B1. Comparison of the average spectrum of V772 Cas (symbols) with the best fitting theoretical model spectrum (solid line). The dotted line shows synthetic spectrum calculated with the solar abundances.

Table B1. Spectral lines employed for determination of abundances in the primary component of V772 Cas. Central wavelengths given with three significant figures correspond to single lines. Wavelengths given with a lower precision indicate lines containing multiple fine, hyperfine and/or isotopic components.

Ion	λ (Å)	Ion	λ (Å)	Ion	λ (Å)	Ion	λ (Å)
Ti II	3913.461	Fe II	4514.516	Fe II	4984.465	He I	5876.6
Ca II	3933.7	Fe II	4515.333	Fe II	4990.506	Si II	5957.559
Fe II	3935.961	Fe II	4520.218	Fe II	5001.953	Fe II	5961.706
Hg II	3983.9	Fe II	4522.628	Fe II	5004.188	Si II	5978.930
Mn II	4000.032	P II	4530.823	S II	5014.042	P II	6024.178
Ni II	4067.031	Si III	4552.622	Fe II	5018.438	P II	6034.039
He I	4120.8	Fe II	4555.887	Fe II	5035.700	P II	6043.084
Fe II	4122.659	P II	4558.095	Si II	5041.024	Ne I	6074.338
Si II	4130.894	Cr II	4558.650	Si II	5055.984	P II	6087.837
S II	4162.665	Ti II	4563.757	Fe II	5061.710	Ne I	6096.163
Ti II	4163.644	Ti II	4571.971	Fe II	5077.896	Mn II	6122.4
Mn II	4164.453	Fe II	4576.333	Mn II	5123.327	Mn II	6128.7
Mn II	4205.3	Si III	4576.849	Fe II	5169.028	Ne I	6143.063
Mn II	4206.3	Fe II	4582.830	Fe II	5197.568	Fe II	6147.734
Mn II	4240.3	Fe II	4583.829	Fe II	5247.956	O I	6155.9
Ga II	4251.154	P II	4589.846	Fe II	5260.254	O I	6158.187
Mn II	4251.7	Cr II	4592.049	Fe II	5275.997	Ne I	6163.594
Mn II	4252.9	P II	4602.069	Mn II	5297.0	P II	6165.598
Mn II	4259.2	Xe II	4603.040	Mn II	5299.3	Ne I	6266.495
C II	4267.2	Cr II	4616.629	Pr III	5299.993	Ga II	6334.9
Fe II	4273.320	Cr II	4618.803	Mn II	5302.4	Ne I	6402.248
Ti II	4290.215	Fe II	4620.513	S II	5320.723	Ga II	6419.1
Mn II	4292.2	Cr II	4634.070	P II	5344.729	P II	6459.945
Fe II	4296.566	Fe II	4635.317	S II	5345.9	P II	6503.398
Ti II	4301.922	He I	4713.1	P II	5409.722	Ne I	6506.528
Mn II	4326.6	Mn II	4727.8	Xe II	5419.150	P II	6507.979
Fe II	4351.762	Mn II	4730.4	Fe II	5427.816	C II	6578.050
Mn II	4356.6	Fe II	4731.448	Fe II	5429.967	C II	6582.580
Mn II	4363.2	Mn II	4755.7	S II	5453.855	Ne I	6598.953
Mn II	4365.2	Mn II	4764.624	S II	5473.614	He I	6678.154
Ti II	4395.031	Mn II	4764.7	Fe II	5482.306	Ne I	6717.043
P II	4420.712	Mn II	4770.3	Fe II	5493.831	Ne I	7032.413
Ti II	4443.801	Mn II	4791.762	P II	5499.697	He I	7065.2
P II	4452.472	Mn II	4806.8	Fe II	5506.199	Mn II	7330.5
P II	4463.027	Cr II	4824.127	Mn II	5559.0	Mn II	7353.3
P II	4475.270	Mn II	4830.061	Mn II	5570.5	Mn II	7367.0
Mn II	4478.6	Xe II	4844.330	Mn II	5578.1	Mn II	7415.8
Mg II	4481.6	Fe II	4921.921	Fe II	5645.390	Mn II	7432.1
Fe II	4489.176	S II	4925.343	Mn II	5826.288	P II	7845.613
Fe II	4491.397	P II	4943.497	S II	5840.1	Mg II	7877.054
Fe II	4508.280	Fe II	4951.581	Ne I	5852.488	Mg II	7896.366